Vision System and Depth Processing for DRC-HUBO+

Inwook Shim[1], Seunghak Shin[1], Yunsu Bok[1], Kyungdon Joo[1], Dong-Geol Choi[1], Joon-Young Lee[2†], Jaesik Park[3†], Jun-Ho Oh[4], and In So Kweon[1]

***Abstract*— This paper presents a vision system and a depth processing algorithm for *DRC-HUBO+*, the winner of the *DRC finals* 2015. Our system is designed to reliably capture 3D information of a scene and objects and to be robust to challenging environment conditions. We also propose a depth-map upsampling method that produces an outliers-free depth map by explicitly handling depth outliers. Our system is suitable for robotic applications in which a robot interacts with the real-world, requiring accurate object detection and pose estimation. We evaluate our depth processing algorithm in comparison with state-of-the-art algorithms on several synthetic and real-world datasets.**

I. Introduction

The need for a robot that can be substituted for a person in certain situation has come to the fore since the Fukushima Daiichi nuclear disaster on March 11, 2011. To counteract the disaster and assist humans in responding to it, the US Defense Advanced Research Project Agency (*DARPA*) held the *DARPA* Robotics Challenge (*DRC*) in 2013 (*trials*) and 2015 (*finals*) [1]. In these events, a robot should carry out diverse tasks with limited human-robot interaction; therefore, recognizing the surrounding environment and objects is one of the fundamental abilities of the robot.

In recent research, depth sensors have been widely used in the computer vision and robotics field, and they open a new horizon for scene understanding [2] and object recognition [3] since they give rich information of a scene in real time. There are various depth sensors, such as stereo-based range sensors, 3D time-of-flight (*3D-ToF*), active pattern cameras (*e.g.Microsift Kinect*), and light detection and ranging sensor (*lidar*). Among them, lidar sensors have a wide measurable range and are also robust to the effects of sunlight; therefore, they are considered the most suitable sensors for outdoor robots.

Although lidar sensors are quite reliable, the depth data from lidar sensors has the form of sparse point clouds, which is typically less than the resolution of an image sensor. In addition, the measured depth may contain depth noise and *flying points* around depth boundaries. These issues make recognizing objects and estimating their poses more challenging while this is one of core techniques for robotics applications. In many cases, the failure of object pose estimation may cause a fatal accident.

To handle these problems, we follow a common principle of depth upsampling, which propagates sparse depth points by utilizing the sharp edge boundaries of the corresponding image. Many studies have been conducted to achieve an accurate and dense depth map from sparse observed points. However, these techniques usually assume that a depth map and image pair is well-aligned and has ignorable alignment error. This assumption is not appropriate, especially for a depth and camera pair that has a wide baseline that is common in robotics applications, because wide baseline sensors generate a large parallax effect to captured data. As a result, the projected depth points in the image domain exhibit *flipping points* and *depth dis-occlusion*.

In this paper, we present a complete system composed of vision sensors and a depth processing algorithm, and show we report its applications in the mission of the *DRC finals* 2015. We designed our sensor system with a pair of a color camera and a lidar. We obtain the 3D structure data of a target area aligned with image information by rotating the sensor. We also propose a new method to obtain a high-resolution depth map by explicitly considering the alignment problem between image and depth data. The key to our upsampling technique includes handling flying points, flipping points, and dis-occlusion region and estimating a confidence map to remove unreliable data. The proposed depth upsampling method was evaluated on benchmark datasets. We also demonstrate real-world robotics applications, such as 3D object pose estimation and toehold detection, which are used for *DRC finals*. Our sensor system and the propose algorithm were adopted for *DRC-Hubo+*, which was declared the winner of the *DRC finals* 2015.

II. Related Work

We review relevant hardware systems and depth processing algorithms that exploit depth sensors and color cameras.

Sensor system Two representative and unveiled sensor systems in the *DRC* used for obtaining visual and geometric information of a scene are: *Team IHMC robotics* [4] and *Tartan Rescue* [5]. *Team IHMC robotics* uses Multisense-SL designed by *Carnegie Robotics* [6]. This sensor system consists of a forward-facing stereo camera and a rotating

This work was supported by Ministry of Trade Industry and Energy of Republic of Korea(MOTIE) (No.10050159) and the National Research Foundation of Korea(NRF) grant funded by the Korea government(MSIP) (No.2010-0028680)

[1]I. Shim, S. Shin, Y. Bok, K. Joo, D.-G. Choi, and I.S. Kweon are with Robotics and Computer Vision Laboratory, Dep. of EE, KAIST, Daejeon, 305-701, Korea {iwshim, shshin, ysbok, kdjoo, dgchoi}@rcv.kaist.ac.kr and iskweon@kaist.ac.kr

[2]J.-Y. Lee is with Adobe Research, San Jose, CA, 95110, United States jolee@adobe.com

[3]J. Park is with Intel Labs, Santa Clara, CA, 95054, United States jaesik.park@intel.com

[4]J.-H. Oh is with Humanoid Research Center, Dep. of ME, KAIST, Daejeon, 305-701, Korea jhoh@kaist.ac.kr

[†]This work was done when they were in KAIST.

axial lidar. In addition, it additionally has two wide-angle cameras to give an operator visual monitoring. *Tartan Rescue* designs their own sensor system, which consists of two lidars, two stereo cameras, and two fisheye cameras.

Depth upsampling Given a depth and color image pair, depth upsampling approaches output a high-quality dense depth map that follows the crisp edge of color images. Joint bilateral upsampling (JBU) [7] applies a spatially varying filter to the sparse samples. The filtering kernels are determined by local color affinity and radial distance. Chan *et al*. [8] accelerated the JBU using a GPU and introduced a depth noise aware kernel. Dolson *et al*. [9] presented a flexible high-dimensional filtering method for increased spatial and temporal depth resolution. Park *et al*. [10], [11] used a least-square cost function that combines several weighting factors with nonlocal structure. Ferstl *et al*. [12] designed smoothness term as a second-order total generalized variation, and propagated sparse seed points using anisotropic diffusion tensor obtained from a high-resolution image.

Among them, filtering approaches [7], [8], [9] have low computational complexity and can be easily parallelized for real-time applications. However, they may not cover large depth holes. This indicates that physically unmeasurable depth samples occur due to dis-occlusion or a distant element of a scene, such as the sky. In contrast, global approaches [10], [11], [12] can fill out large depth holes because all of the depth variables in the cost function are densely connected. However, they may also propagate erroneous observations to a large area.

Depth outliers handling In practice, sparse seed points used for depth upsampling may contain outliers. This is because of *flipping points* and *depth dis-occlusion* that occurs when the measured range data is projected onto the image domain. In addition, there are *flying points*, which indicate intermediate depth values between foreground and background depths occurring around object boundaries. To overcome these challenges, Kang *et al*. [13] detected the flipping points based on the distribution of depth values within a color image segment. Park *et al*. [10] measured depth variation of the local regions, which is for detecting depth discontinuity. Those discontinuity candidate regions are refined via binary label optimization. An extended work [11] proposed a heuristic approach that detects flipped depth orders after depth projection. However, their work evaluated the performance of their algorithm on exactly-aligned depth-color image pairs. To a wider extent, ToF depth camera and stereo color camera fusion [14], [15] were also introduced. Gandhi *et al*. [15] looked for small regions that have mixed foreground and background depth samples. Georgios *et al*. [14] grew seeds using a smoothness term that is conditionally defined by an occlusion label obtained from depth discontinuity analysis.

In this paper, we focus on practical issues of an image and depth capturing system and depth processing for robot applications. We introduce sensor calibration for our vision system, depth outliers handling, and depth map upsampling.

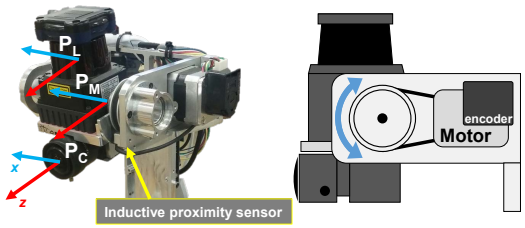

Fig. 1: Sensor system configuration (left) and an example of its movement (right). lidar and camera are placed on the same plate, which is rotated by a single motor.

Our filter based approach can generate a high-quality and outliers-free depth map that is capable of accurate object detection and pose estimation. Our depth outliers rejection stage is not dependent on the edge information of the image; therefore, it keeps reliable points even in ambiguous image edges. In addition, our confidence map explicitly disregards large holes in a depth map and propagates reliable samples.

III. Sensor System

A. System Configuration

Fig. 1 shows our sensor system which consists of one lidar sensor, one *GigE* camera, and one stepper motor with an incremental encoder. The camera equipped with a 2.2 *mm* lens has 1288×964 resolution with a $118.6^\circ\times90.0^\circ$ field-of-view (FoV). The motor with a high resolution encoder provides angle information in 0.02 degree resolution. The motor finds its zero reference position by checking the signal of the inductive proximity sensor.

This system acquires 3D points by rotating the lidar sensor around the motor's x-axis and captures an image at each target angle. We can control the rotation scope, rotation speed, and target angle using our control software, therefore we can control the sparsity of 3D points by trading off capturing time when we reconstruct the 3D structure of a target area. We also adjust the camera exposures to maximize image features [16].

B. System Calibration

The sensor system should be calibrated in the robot coordinate so that captured data can be utilized for robot applications. We divide the whole calibration process into three steps: (1) camera intrinsic, (2) camera and motor, and (3) camera and lidar extrinsic.

The first step, camera intrinsic calibration, is done by a conventional method using a planar checkerboard pattern [17]. To account for the short focal length of the lens, the conventional model adopts a fisheye distortion model [18]:

$$\begin{bmatrix} x_d \\ y_d \end{bmatrix} = \frac{\tan r}{r} \begin{bmatrix} x \\ y \end{bmatrix}, \tag{1}$$

$$r = \sqrt{x^2 + y^2}, \tag{2}$$

where $[x\ y]^\top$ and $[x_d\ y_d]^\top$ denote the ray directions in the camera coordinate system ($z = 1$) before and after distortion, respectively. The model is derived from the equidistant

model among the mapping functions of fisheye lenses [18]. However, the model can not reduce the projection error sufficiently. We modify the distortion model of the fisheye lens by adding additional parameter k to r:

$$r' = k\sqrt{x^2+y^2}, \tag{3}$$

where k is an unknown distortion parameter. Substituting Eq. (2) with Eq. (3), the mean projection error is reduced from 1.692 pixels to 0.360 pixels, where the value of k is estimated as 0.9413. Other toolboxes for obtaining intrinsic parameters of fisheye lenses also allow precise results [19][20][21].

For the next two steps, we designed a pattern that consists of two perpendicular checkerboard patterns, rather than using a single pattern. Scan data on both planes are extracted and used to estimate the relative pose between a camera and a lidar sensor as follows.

For each pose of the pattern, we capture images for every 10 degrees of motor rotation. Although we use a high-accuracy step motor, we assume that only its repeatability (not its angular accuracy) is reliable. The rotation angles of images are considered unknown values, rather than fixed-value constraints. Let A_θ be the unknown angle corresponding to the motor angle θ computed by counting motor steps. In our implementation, the angle θ varies from -30 to 80 degrees so that we add 11 unknown variables $A_{-30} \sim A_{80}$ corresponding to 12 angles. It should be noted that A_0 is fixed to zero as the reference angle. Because we set the rotation axis of the motor as the x-axis of the motor coordinate system, the rotation matrix $\mathbf{R}_\theta$ is compute as follows:

$$\mathbf{R}_\theta = \begin{bmatrix} 1 & 0 & 0 & 0 \\ 0 & \cos A_\theta & \sin A_\theta & 0 \\ 0 & -\sin A_\theta & \cos A_\theta & 0 \\ 0 & 0 & 0 & 1 \end{bmatrix}. \tag{4}$$

We capture the images of the pattern in N different poses. The number of images may vary between poses due to the limitation of the camera's FoV. Let K_n be the number of frames captured in the n-th pose. The cost function f_c for the estimation of the motor-to-camera transformation $\mathbf{H}_{mc}$ is the projection error of feature points on the perpendicular patterns:

$$f_c(\mathbf{H}_{mc}, \mathbf{H}_1 \sim \mathbf{H}_N, A_{-30} \sim A_{80}) = \sum_{n=1}^{N}\sum_{k=1}^{K_n}\sum_{i} \|\mathbf{q}_i - proj(\mathbf{H}_{mc}\mathbf{R}_\theta\mathbf{H}_n\mathbf{p}_i)\|^2, \tag{5}$$

where $\mathbf{H}_n$ denotes the transformation from the pattern in the n-th pose to the motor, and $proj(\cdot)$ indicates the process of the projection from camera to image, including radial distortion. $\mathbf{p}_i$ and $\mathbf{q}_i$ represent feature points of the patterns and its location in the image, respectively. Because the pattern-to-motor and motor-to-camera transformations compensate each other, we fix both rotation and translation of the motor-to-camera transformation along the x-axis as zero.

The last step, camera-lidar calibration, is easily done by utilizing the results of the previous step. Because we have already estimated the pattern-to-camera transformation for every image, we simply adopt the constraint that lidar scanning points must lie on the corresponding patterns [22]. The cost function f_l of the estimation of the lidar-to-camera transformation $\mathbf{H}_{lc}$ is the distance between the lidar scanning points and planar patterns:

$$f_l(\mathbf{H}_{lc}) = \sum \left(\mathbf{v}_z^\top \mathbf{H}_{pc}^{-1}\mathbf{H}_{lc}\hat{\mathbf{p}}\right)^2, \tag{6}$$

where $\hat{\mathbf{p}}$ indicates the lidar scanning points on the patterns. We adopt the z-axis unit vector $\mathbf{v}_z = [0\ 0\ 1\ 0]^\top$ to consider only the z-terms of the points because we set each planar pattern as $z = 0$ of its own pattern coordinate system.

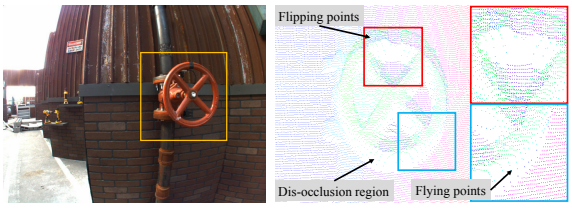

Fig. 2: Images showing parallax effects. Left image shows a target region, and right image depicts registered 3D points to the camera coordinate, P_C.

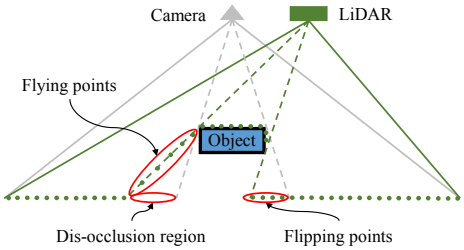

Fig. 3: Example showing why flying and flipping points as well as, dis-occlusion problems occur in depth and image alignment.

IV. Depth Processing

With our system, we can capture dense 3D information by keeping the motor rotation speed slow. However, it is important to capture *high quality* 3D information within a reasonable *time budget* for the *DRC finals* since we should carry out the tasks quickly with limited human-robot interaction. To satisfy the conflicting requirements, we adjust the motor rotation speed to be suitable for human-robot interactions and perform depth upsampling to complement sparse raw depth measurements using a high-resolution image.

The first step for depth upsampling is to align a depth and image pair. We align them by projecting depth measurements into the image domain using the calibration parameters. We show an example of the alignment in Fig. 2. As shown in the figure, there are several erroneous depth points due to the factors depicted in Fig. 3.

Flying points are caused by the measurement noise of depth sensors around object boundaries. Flipping points occur when the camera cannot see the corresponding region due to occlusion. Though they are regular points in the

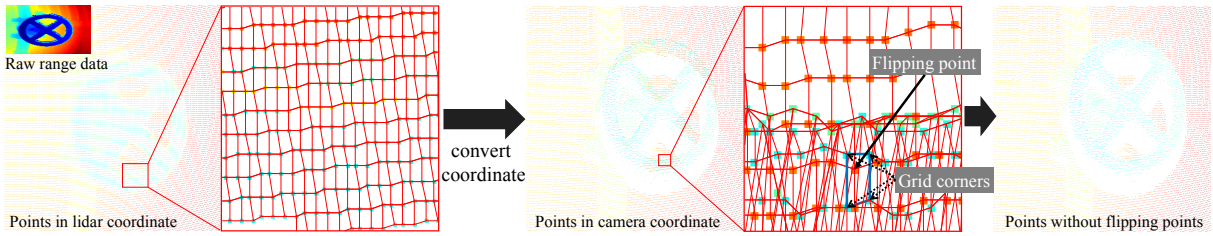

Fig. 4: Pipeline for eliminating flipping points using a 4-connected grid map. The flying and sparse points are removed in advance using the method described in Section IV-A.

lidar coordinate, they are projected onto the occluding object region in the image coordinate. The dis-occlusion region is the opposite case of the flipping points. There is no true depth measurement due to occlusion. These alignment problems are amplified due to system calibration error and measurement noise of the depth sensor. In all image-guided depth upsampling algorithms, the unreliability of the aligned measurements severely degrades the performance of depth upsampling as will be discussed in the Section V.

Therefore, we have to handle this unreliability explicitly before performing depth upsampling. We remove flying points if two adjacent points along a lidar scan-line have a large distance between them, and we then apply a 2D filter to eliminate isolated sparse points from the image domain. We also remove flipping points by checking the depth information among nearby points. After removing the suspicious points, we run our depth upsampling and generate a confidence map concurrently. Then, we use a confidence map to distinguish low reliability regions that include dis-occlusion. We describe this in greater detail in the following sections.

A. Flying Point Rejection

Flying points commonly occur around object boundaries since lidar measurements are noisy when the surface geometry is unstable. To remove flying points, we use a simple 1D filter as follows:

$$P_f = \{x | max(d(x_t^l, x_{t-1}^l), d(x_t^l, x_{t+1}^l)) > T_f\}, \tag{7}$$

where P_f is a set of flying points, $d(\cdot)$ is the Euclidean distance between two points, x_t^l is the t-th point in an l-th scan-line. Here, T_f is a predefined threshold, which was empirically set to $30mm$ in our experiment. This filter is applied to each lidar scan-line. After that, we use morphological operations in the image to remove isolated sparse points.

B. Flipping Point Rejection

Most depth upsampling methods assume that the pair of a high-resolution image and a low-resolution depth map is well aligned, and they do not treat flipping points problem seriously. In real environments, the flipping points pose a serious problem in depth upsampling; therefore, we should account for it.

Fig. 4 shows the process for eliminating flipping points. We first generate a 4-connected grid map from depth measurements in the lidar coordinate. Each cell in the grid map is composed of four corner points. Then, we move the grid map to the camera coordinate, and find the points that invade into another grid cell as shown in the center image of Fig. 4. Among the points, we reject a point if its depth is more distant than the depth of each corner point of the invaded grid cell. A depth map produced after the rejection of flipping points is shown in the right image in Fig. 4.

C. Depth Map Upsampling and Confidence Map Estimation

In this section, we describe our depth upsampling algorithm. We also explain how to compute a confidence map and determine parameters.

1) Depth Map Upsampling: For robotics applications, such as object detection and pose estimation, we upsample a captured depth map with the guidance of an aligned image. Our depth upsampling algorithm is based on a rolling guidance filter suggested by Zhang *et al.* [23]. The rolling guidance filter is an iterative joint filter method that can achieve scale-aware local operations; therefore, it is especially useful for removing small-scale structures such as noise while performing edge-preserving upsampling.

In our upsampling algorithm, we extend the JBU [7] with an additional depth guidance term to prevent the texture copying problem and use the extended JBU as a joint filter in the rolling guidance filter. Specifically, our upsampling algorithm is formulated as follows:

$$\begin{aligned} D_p^{t+1} &= \frac{1}{N_p} \sum_{q \in \Omega(p)} exp(G_{p,q} + K_{p,q} + H_{p,q}) R_q, \\ \text{s.t.} \quad G_{p,q} &= -\|p-q\|^2 / 2\sigma_s^2, \\ K_{p,q} &= -\|I_p - I_q\|^2 / 2\sigma_i^2, \\ H_{p,q} &= -\|D_p^t - R_q\|^2 / 2\sigma_d^2, \\ N_p &= \sum_{q \in \Omega(p)} exp(G_{p,q} + K_{p,q} + H_{p,q}), \end{aligned} \tag{8}$$

where I, R, and D^t denote a guidance image, an aligned sparse depth map, and an upsampled dense depth map after the t-th iteration, respectively. Here, p is a query point in the 2D image coordinate, and $\Omega(p)$ is a set of neighboring points from R within a filter range. We use only sparse points $\Omega(p)$ from R as supporting pixels for efficient computation. σ_s, σ_i, and σ_d denote the standard deviations to control the influence each of the spatial similarity term G, the intensity similarity term K, and the depth similarity term H, on the filter weights, and N_p is a normalization factor of the weights. For an initial upsampled depth map D^0, we use the JBU [7] where H is set to zero in Eq. (8).

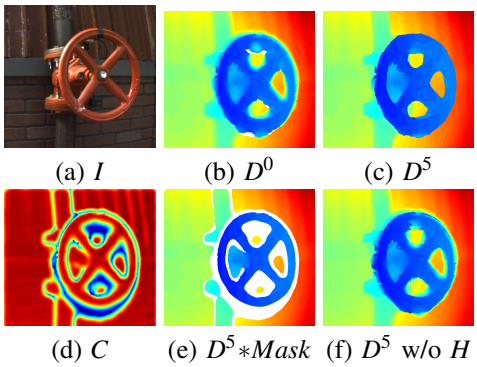

(a) I (b) D^0 (c) D^5

(d) C (e) $D^5 * Mask$ (f) D^5 w/o H

Fig. 5: Intermediate results of our upsampling method. (a) Input image, (b) Initial depth map D^0, (c) Our result after 5 iterations, (d) Confidence map, (e) Our result after masking low reliability regions in white. (f) Upsampling result without the H term.

Eq. (8) iteratively enhances an estimated dense depth map, D^t. In the scheme, the depth guiding term H has an important role. Using the aligned raw depth measurements R, where outliers are effectively rejected, H suppresses error propagation and texture copying problems, which often occur in the JBU. Also, it gives key information in computing the confidence of an estimated depth map.

Fig. 5 shows the intermediate result of our upsampling method. In the figure, our result after five iterations in (c) has sharper and more accurate depth boundaries than an initial upsampled depth map in (b), while the result without the H term in (f) has noisy depth boundaries due to overfitting to intensity information.

2) Confidence Map Estimation: In our configuration that cannot ignore the baseline between depth and image sensors, ambiguity regions may exist in the upsampling results due to a lack of true measurements like dis-occlusion as shown in Fig. 3. While it is very difficult to solve the problem during the upsampling process, it can be effectively handled by computing a confidence map from the upsampling filter weights.

The confidence of depths is closely related to the statistics of measurements where small variance of local supporting measurements raises the confidence of the resulting depth. Therefore, we define the confidence measure C of an upsampled depth value on the location p as

$$C_p = \sum_{t=0}^{n} \Big(\sum_{q \in \Omega(p)} exp(G_{p,q} + H_{p,q}) \Big), \tag{9}$$

where n is the number of iterations, and other notations are the same as Eq. (8). This confidence measure is simultaneously computed during processing of our upsampling algorithm. The notion behind this measure is that a pixel has low confidence if the estimated depth is supported by few or unstable depth measurements. From the measure, we mask an estimated depth out as an unreliable result if its confidence value is lower than $0.35 \times max(C)$.

Fig. 5-(d) shows our confidence map, and (e) is the upsampling result with a confidence mask. As shown in the figure, our confidence mask effectively removes the unreliable regions around depth boundaries due to parallax effects and retains important depth information with clean and sharp depth boundaries.

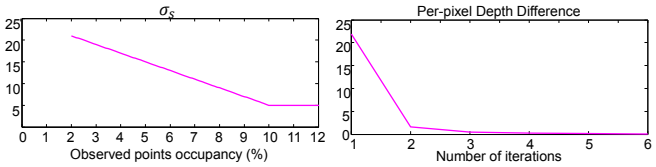

(a) Spatial smoothness parameter (b) Number of iterations

Fig. 6: Parameter selection

3) Parameter Selection: We have several parameters to perform our depth upsampling. First, σ_s is a spatial smoothness parameter, and we adaptively determined it through empirical cross-validation since the proportion of measured depth points to the guidance image pixels may vary according to the rotation speed of our system. Fig. 6-(a) shows the parameter we used according to the proportion. For example, if the measured points occupy 5% of a guided image area, σ_s is set to 15. To guarantee the quality of our upsampling result, we control the maximum rotation speed of our sensor system to secure at least 2% of the proportion.

Next, σ_d is a depth similarity parameter to suppress depth measurement noise. We determined σ_d according to the specification of our lidar sensor, *UTM 30LX-EW*. Because the maximum repeated accuracy of the lidar sensor is less than $\pm 30mm$, we set σ_d to 30. We empirically set the intensity similarity parameter σ_i to 20.

We also need to determine the number of iterations in the rolling guidance scheme. We computed the average depth variations at each iteration step with an example dataset, and the results are shown in Fig. 6-(b). As stated in the original paper [23] of the rolling guidance filter, the depth map rapidly converges to the final result within 3∼5 iterations.

V. Experimental Results

To validate the performance of the proposed algorithm including depth outliers rejection, depth upsampling, and confidence map, we performed experiments on both synthetic and real datasets, and compared our method to state-of-the-art methods, such as total generalized variation (TGV) [12], nonlocal means (Nonlocal) [10], and joint bilateral filter (JBU) [7]. For the experiments, we used two computers, namely, a data capturing machine equipped with a 1.3GHz dual-core CPU and 8GB RAM, and a depth processing machine equipped with a 3.6GHz quad-core CPU and 16GB RAM. Our CPU-based implementation takes less than a second to generate a dense depth map of 640×480 resolution with five iterations of joint filtering.

A. Middlebury Evaluation

For a quantitative evaluation, many previous researchers have assumed that the pair of depth and image is exactly aligned [12], [10], [7]. In practice, there are many sources

TABLE I: Quantitative comparison results. The detailed description is shown in Section V-A.

Dataset	Adirondack		Bicycle1		Classroom1		Flowers		Motorcycle		Storage		Umbrella		Vintage	
Error metric	A80	A95	A80	A95	A80	A95	A80	A95	A80	A95	A80	A95	A80	A95	A80	A95
TGV [12]	19.6	152.3	14.5	86.8	40.2	364.3	64.5	1028.0	32.0	388.9	44.9	723.2	32.9	259.5	40.3	403.8
Nonlocal [10]	9.7	285.9	9.1	183.7	6.3	99.0	125.5	682.2	29.7	471.8	86.1	1084.8	8.2	229.4	8.9	84.5
Bilateral [7]	4.7	160.5	4.4	116.0	4.4	21.0	7.5	575.6	7.5	379.0	4.9	448.4	4.6	89.8	4.3	17.1
Ours w/o C	4.0	8.4	**3.6**	8.0	3.6	9.0	3.7	7.6	5.7	15.5	3.9	10.4	3.6	7.4	4.6	8.1
Ours	**3.3**	**7.0**	4.5	**6.4**	**3.2**	**6.3**	**3.3**	**5.7**	**5.0**	**9.9**	**3.6**	**7.9**	**3.5**	**6.4**	**4.4**	**7.5**

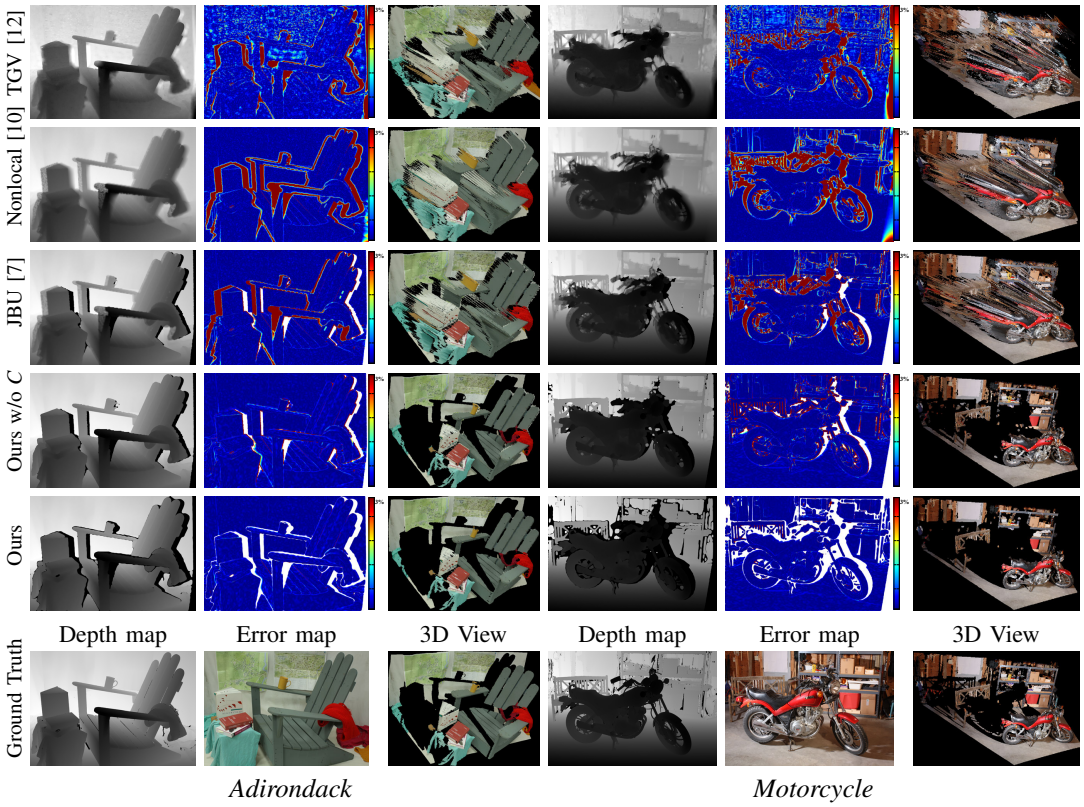

Fig. 7: Examples of upsampling results described in Section V-A. "Ours w/o C" denotes our upsampling method without the confidence map. The error maps depict a relative depth error ranging from 0 to the 3% of the maximum depth. The white pixels in the error maps were excluded when the results in Table I were computed. We used $\sigma_s = 20$ pixels, $\sigma_i = 20$ pixels, and $\sigma_d = 30mm$ for the experiment.

of alignment error, including measurement noise, system calibration error, flying and flipping points, and dis-occlusion; therefore, the aligned sparse depth samples on the image domain exhibit severe flipping as described in Fig. 2.

To tackle the problem, we designed a new testbed based on the Middlebury stereo 2014 datasets [24]. Each dataset in [24] consists of high-resolution stereo images, ground-truth depth maps estimated using a structured lighting system, and calibration parameters. In our testbed, we simulated the depth and image measurements as follows. First, we sampled the ground-truth depth pixels on the left view by every 4 pixels in a column and 12 pixels in a row to simulate the asymmetric density of depth measurements of our system. We added additive Gaussian noise ($\sigma = 10mm$) to the samples. Then, the noisy depth samples were projected onto the right view. The aligned depth points cover about 2% of the image resolution. In total, we generated 23 test datasets from all the Middlebury stereo 2014 datasets with ground-truth. Although we used the ground-truth calibration parameters, the dataset generated from our testbed naturally exhibits flying points, flipping points, and dis-occlusion problems similar to the dataset captured from our real system.

For a quantitative comparison, we used a robust accuracy measure, "AN" as used in [25]; "AN" denotes the depth error at the N-th percentile after the errors are sorted from low to high. We used the hole-filled results for the global methods [12], [10], while for the local methods, JBU [7] and ours, we excluded the mask regions that could not compute results with local filters due to large holes or low confidence.

Table I shows the quantitative comparison results. Our method worked consistently well in the configurations both of A80 and A95, while the performance of the other methods were exponentially degraded in A95. The upsampling results and error maps are also shown in Fig. 7. Compared to our method, the other methods showed large errors and suffered from severe artifacts at the depth boundary regions that are clearly seen in the 3D view in the figure.

Major benefit of our approach is that it offers a novel depth

outliers rejection scheme that gives clear seed depth points. In addition, our scale-aware depth upsampling gives more tolerance on the noisy depth measurements in homogeneous surfaces. The remaining ambiguous depth pixels adhered to the boundary region of a large structure are effectively rejected by our confidence map. The 3D views in Fig. 7 also show that our results successfully preserve depth discontinuity and its fine structures. More quantitative and qualitative results are presented in the supplemental material[1].

B. DRC finals 2015

Our depth upsampling algorithm was utilized for the part of DRC tasks, namely, object detection and pose estimation of real-world objects. In the tasks, it was important to obtain a dense and accurate depth map to successfully recognize the 3D poses of target objects for grasping. In practice, raw depth data from lidar was too sparse and noisy to accurately estimate the pose of an object. Our depth upsampling method is able to generate a high-quality depth map that improves the success-rate of each task.

We developed task-specific detection algorithms for three target objects: valve, drill, and terrain. In the VALVE and DRILL cases, we initially set a region of interest for a target object. Then our pose estimation algorithms estimate the 3D pose of a target object by fitting predefined 3D templates to a depth map. In the TERRAIN case, each local plane is detected by progressive grouping of surface normal directions. Then, the groups are refined using Graph Cut [26].

We performed the tasks with several depth map variants, such as a raw depth map, our upsampling result, and state-of-the-art upsampling results of [12], [10], [7]. Fig. 8 shows a qualitative comparison of the upsampled depth maps. Fig. 9 visualizes the results of object detection and pose estimation. Our algorithm estimates an accurate and outliers-free depth map with sharp depth boundaries. Our depth map results in accurate 3D template fitting while the other tested variants may fail to accurately detect the poses of objects. Especially in the DRILL example, pose estimation is challenging because of the lack of valid points and depth error existing at the object boundaries. Using our depth map, the desirable grasping direction is correctly determined. In the case of TERRAIN detection, accurate estimation of surface normal is important for robot treading. Our method results in the most accurate pose estimation without any missing block.

VI. CONCLUSIONS

We have presented a vision system including a calibration and a depth processing method that are specially designed for robust and reliable depth sensing. Our depth processing method explicitly handles noisy or unreliable depth observations; therefore, it outputs a high-fidelity dense depth map. Through intensive evaluations, we verified that our method outperforms state-of-the-art methods and demonstrated that our method is especially suitable for robotics applications.

[1] https://sites.google.com/site/iwshimcv/home

REFERENCES

[1] "Darpa robotics challenges finals 2015." [Online]. Available: http://www.theroboticschallenge.org/

[2] F. Endres, J. Hess, N. Engelhard, J. Sturm, D. Cremers, and W. Burgard, "An evaluation of the rgb-d slam system," in *IEEE International Conference on Robotics and Automation*, 2012, pp. 1691–1696.

[3] S. Gupta, R. Girshick, P. Arbeláez, and J. Malik, "Learning rich features from rgb-d images for object detection and segmentation," in *European Conference on Computer Vision*, 2014, pp. 345–360.

[4] M. Johnson, B. Shrewsbury, S. Bertrand, T. Wu, D. Duran, M. Floyd, P. Abeles *et al.*, "Team ihmc's lessons learned from the darpa robotics challenge trials," *Journal of Field Robotics*, pp. 192–208, 2015.

[5] A. Stentz, H. Herman, A. Kelly, E. Meyhofer, G. C. Haynes, D. Stager, B. Zajac, J. A. Bagnell *et al.*, "Chimp, the cmu highly intelligent mobile platform," *Journal of Field Robotics*, pp. 209–228, 2015.

[6] "Carnegie robotics." [Online]. Available: http://carnegierobotics.com/

[7] J. Kopf, M. F. Cohen, D. Lischinski, and M. Uyttendaele, "Joint bilateral upsampling," *ACM Trans. on Graphics*, vol. 26, no. 3, 2007.

[8] D. Chan, H. Buisman, C. Theobalt, and S. Thrun, "A noise-aware filter for real-time depth upsampling," in *Workshop on Multi-camera and Multi-modal Sensor Fusion Algorithms and Applications*, 2008.

[9] J. Dolson, J. Baek, C. Plagemann, and S. Thrun, "Upsampling range data in dynamic environments," in *IEEE Conference on Computer Vision and Pattern Recognition*, 2010, pp. 1141–1148.

[10] J. Park, H. Kim, Y.-W. Tai, M. S. Brown, and I. Kweon, "High quality depth map upsampling for 3d-tof cameras," in *IEEE International Conference on Computer Vision*, 2011, pp. 1623–1630.

[11] J. Park, H. Kim, Y.-W. Tai, M. S. Brown, and I. S. Kweon, "High-quality depth map upsampling and completion for rgb-d cameras," *IEEE Trans. on Image Processing*, vol. 23, no. 12, 2014.

[12] D. Ferstl, C. Reinbacher, R. Ranftl, M. Rüther, and H. Bischof, "Image guided depth upsampling using anisotropic total generalized variation," in *IEEE International Conference on Computer Vision*, 2013.

[13] Y.-S. Kang and Y.-S. Ho, "Efficient up-sampling method of low-resolution depth map captured by time-of-flight depth sensor," in *Asia-Pacific Signal and Information Processing Association Annual Summit and Conference*, 2013, pp. 1–4.

[14] M. H. Georgios D. Evangelidis and R. Horaud, "Fusion of range and stereo data for high-resolution scene-modeling," *IEEE Trans. on Pattern Analysis and Machine Intelligence*, 2015.

[15] J. C. Vineet Gandhi and R. Horaud, "High-resolution depth maps based on tof-stereo fusion," in *IEEE International Conference on Robotics and Automation*, 2012, pp. 4742–4749.

[16] I. Shim, J.-Y. Lee, and I. S. Kweon, "Auto-adjusting camera exposure for outdoor robotics using gradient information," in *IEEE/RSJ International Conference on Intelligent Robots and Systems*, 2014.

[17] Z. Zhang, "A flexible new technique for camera calibration," *IEEE Transactions on Pattern Analysis and Machine Intelligence*, vol. 22, no. 11, pp. 1330–1334, 2000.

[18] Y. Xiong and K. Turkowski, "Creating image-based vr using a self-calibrating fisheye lens," in *IEEE Conference on Computer Vision and Pattern Recognition*, 1997, pp. 237–243.

[19] J.-Y. Bouguet, "Camera calibration toolbox for matlab," 2004.

[20] J. Kannala and S. S. Brandt, "A generic camera model and calibration method for conventional, wide-angle, and fish-eye lenses," *IEEE Trans. on Pattern Analysis and Machine Intelligence*, pp. 1335–1340, 2006.

[21] D. Scaramuzza, A. Martinelli, and R. Siegwart, "A toolbox for easily calibrating omnidirectional cameras," in *IEEE/RSJ International Conference on Intelligent Robots and Systems*, 2006, pp. 5695–5701.

[22] Q. Zhang and R. Pless, "Extrinsic calibration of a camera and laser range finder (improves camera calibration)," in *IEEE/RSJ International Conference on Intelligent Robots and Systems*, vol. 3, 2004.

[23] Q. Zhang, X. Shen, L. Xu, and J. Jia, "Rolling guidance filter," in *European Conference on Computer Vision*, 2014, pp. 815–830.

[24] D. Scharstein, H. Hirschmüller, Y. Kitajima, G. Krathwohl, N. Nešić, X. Wang, and P. Westling, "High-resolution stereo datasets with subpixel-accurate ground truth," in *Pattern Recognition*, 2014.

[25] S. Baker, D. Scharstein, J. Lewis, S. Roth, M. J. Black, and R. Szeliski, "A database and evaluation methodology for optical flow," *International Journal of Computer Vision*, vol. 92, no. 1, pp. 1–31, 2011.

[26] Y. Boykov and O. Veksler, "Graph cuts in vision and graphics: Theories and applications," in *Handbook of mathematical models in computer vision*. Springer, 2006, pp. 79–96.

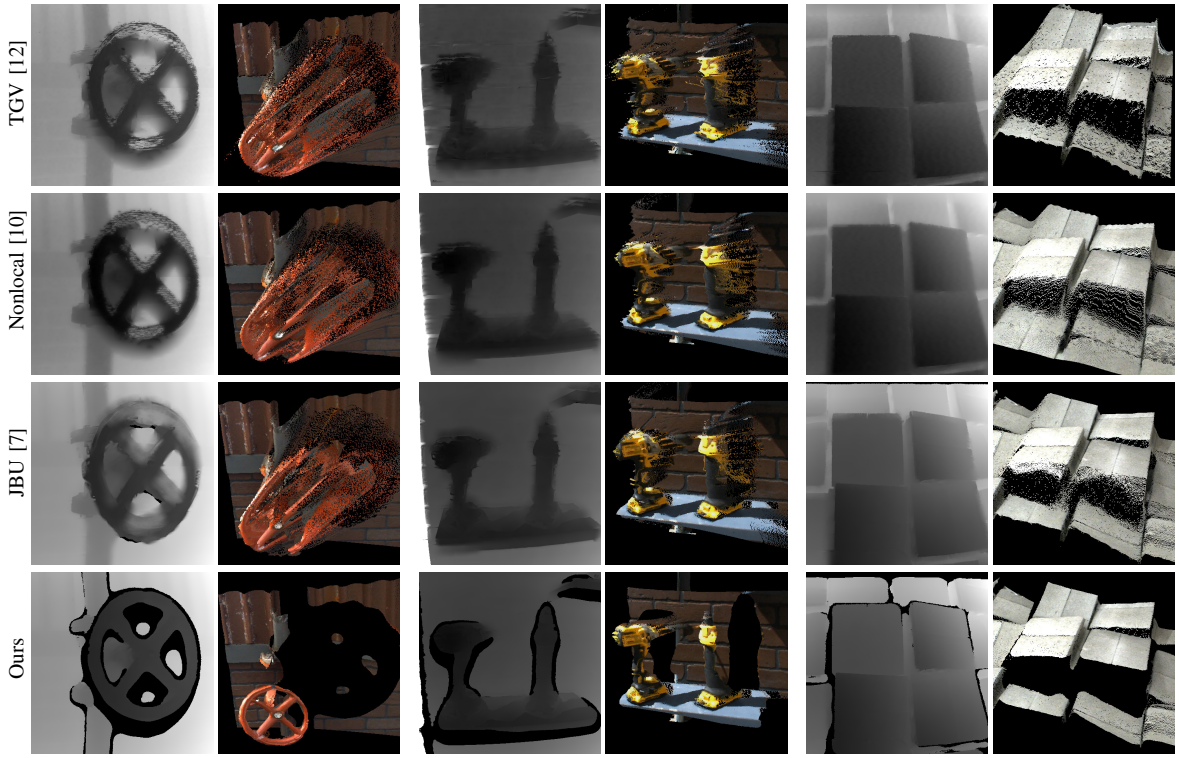

(a) VALVE (b) DRILL (c) TERRAIN

Fig. 8: Qualitative comparison of upsampled depth maps on the *DRC finals* 2015 datasets: VALVE, DRILL, and TERRAIN. The sparse depth observations acquired from lidar are propagated to generate dense depth maps. Note that clear depth boundaries observable in our results.

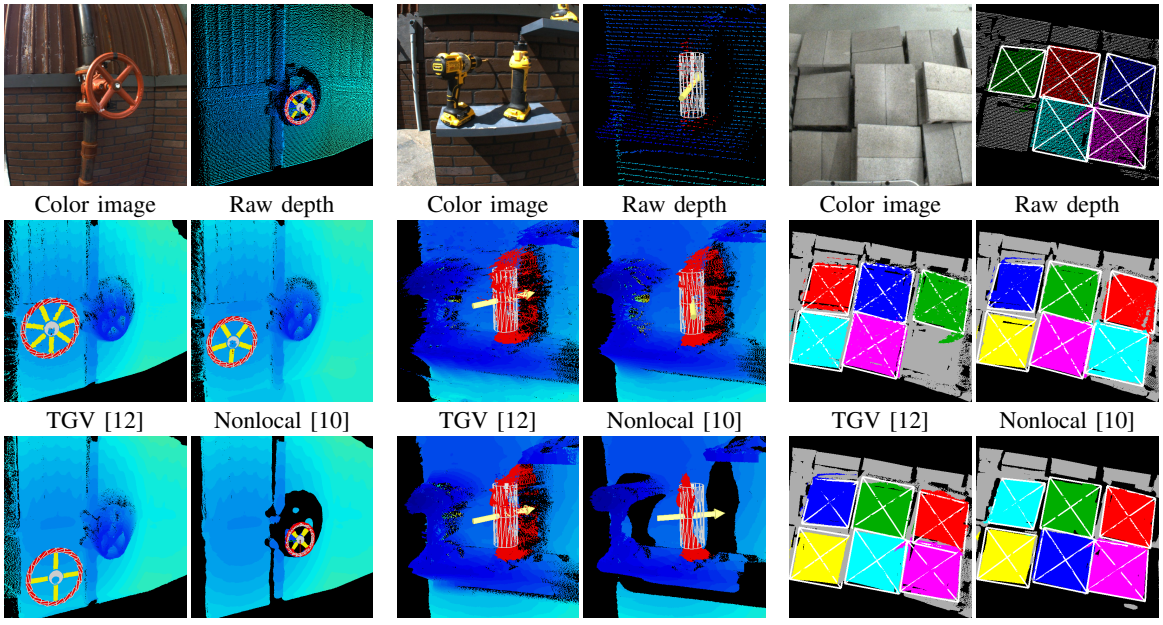

(a) VALVE (b) DRILL (c) TERRAIN

Fig. 9: Object detection and pose estimation using various depth maps. (a) VALVE. The 3D template is correctly aligned with our depth map. Note that our pose estimation approach evaluates several templates having different number of spokes and scales. (b) DRILL. The raw depth is too sparse, and it suffers from flying pixels. Although body part (white cylinder) are detected in every depth maps, the yellow arrow indicating grasping direction is correctly detected (corresponds to the dark part of the right drill in the color image) in our depth map. (c) TERRAIN. The colored points indicate the detected cinder blocks, and white rectangles denote the estimated pose of detected blocks.